Electronic Supplementary Material (ESI) for Materials Horizons.

Supplementary Information

Superhydrophobic Microstructures for Better Anti-Icing Performances: Open-Cell or Closed-Cell?

*Lizhong Wang[1], Guochen Jiang[1], Ze Tian[1], Changhao Chen[1], Xinyu Hu[1], Rui Peng[1], Hongjun Zhang[1], Peixun Fan[1] and Minlin Zhong[1]**

[1]Laser Materials Processing Research Center, Key Laboratory for Advanced Materials Processing Technology (Ministry of Education), Joint Research Center for Advanced Materials & Anti-icing of Tsinghua University (SMSE)-AVIC ARI, School of Materials Science and Engineering, Tsinghua University, Beijing 100084, P. R. China

Correspondence to: zhml@tsinghua.edu.cn

This Supplemental Information includes:

S1. Laser fabricating parameters of patterned micro-nanostructures

S2. Superhydrophobicity characterization of patterned micro-nanostructures

S3. Superhydrophobic durability tests of different patterned surfaces at room temperatures

S4. Constructed thermodynamically closed systems and open systems on patterned surfaces

S5. Icing & melting cycles on different patterned surfaces

S6. Calculation of air pocket pressures on the open-cell structures and the closed-cell structures

S7. Calculation of interfacial thermal resistances on different patterned surfaces

S8. Calculation of total bubbles volume in the ice droplet

S9. Icing & melting cycle tests on copper substrates

S10. Durability analyses of different patterned surfaces after multiple deicing cycles

S11. Observations of condensation processes on open-cell structures.

Other Supplementary Materials for this paper include:

Movie S1: Icing & melting cycle on different patterned surfaces (MP4)

Movie S2: Ice adhesion strengths on the closed-cell and the open-cell surfaces (MP4)

Movie S3: Condensation frosting processes (MP4)

S1. Laser fabricating parameters of patterned micro-nanostructures

The laser processing parameters of patterned micro-nanostructured surfaces are presented in Table S1. The micro-nanostructrued topologies of surfaces are shown in Figure 1f. By adjusting the laser scanning paths (Figure S1), the patterns can be facilely tuned. Under the same processing parameters, the microstructure heights and intervals of different patterned surfaces are fixed at 45 μm and 35 μm, respectively.

Table S1. Laser processing parameters for fabricating micro-nanostructures.

Processing	Laser Fluence (J/cm^2)	Scanning Speed (mm/s)	Repetition Rate	Pulse Duration	Scanning Route	Scanning Pitch (μm)
One Irradiation	0.5-3.8	300-600	200kHz	800fs	Line Scanning	35

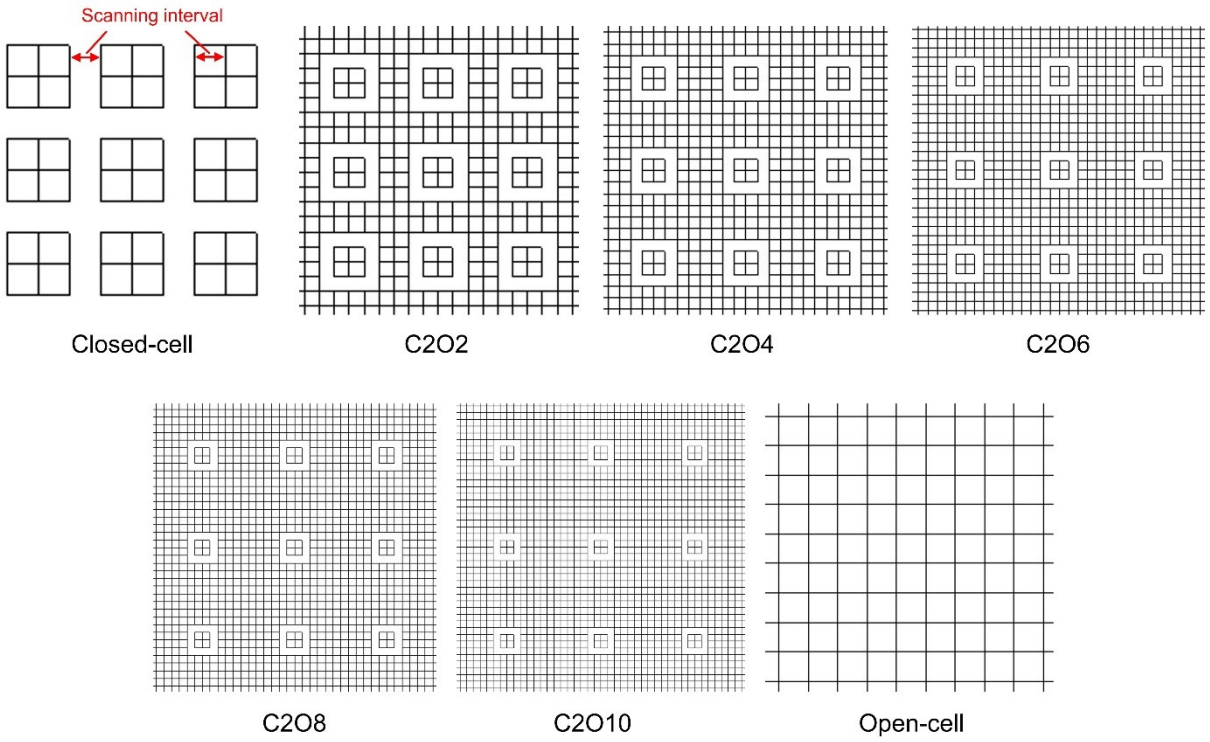

Fig. S1 Laser scanning paths realizing the fabrication of tunable patterned micro-nanostructures

S2. Superhydrophobicity characterization of patterned micro-nanostructures

In terms of structural characteristics, the solid fractions of different surfaces can be expressed by:

$$f = \begin{cases} \dfrac{(i^2-1)B^2 + 2(i+1)B\Lambda}{(i+1)^2\Lambda^2} & (Closed\ cell, j=0) \\ \dfrac{\left[(i+j)^2+4j\right]B^2 + 4(i+1)B\Lambda}{(2+i+j)^2\Lambda^2} & (Hybrid\ cell, i, j \neq 0) \\ \dfrac{B^2}{\Lambda^2} & (Open\ cell) \end{cases} \quad \text{(S1)}$$

where i and j denote the number of microcones in the microframes and outside the microframes of ^{C_iO_j} surfaces, respectively; B is the peak width of microcones; Λ is the periodical distance of microcones. The solid fractions and contact angles of different surfaces are shown in Table S2 and Figure S2.

Table S2. Solid fractions and superhydrophobicity of different micro-nanostructures. Open-I35 and Open-I45 surfaces denote the open-cell surfaces with the same microcone height of 45 μm but different microcone intervals of 35 μm and 45 μm, respectively.

Types	ROTs	Solid fractions f	Apparent contact angle θ_0	Receding angle θ_r	Advancing angle θ_a
Closed	0	0.081	$158.4° \pm 1.2°$	$157.7° \pm 0.6°$	$162.3° \pm 0.7°$
C2O2	0.56	0.047	$159.5° \pm 0.8°$	$157.8° \pm 1.1°$	$162.1° \pm 0.5°$
C2O4	0.75	0.032	$159.3° \pm 0.7°$	$158.4° \pm 1.9°$	$161.9° \pm 2.5°$
C2O6	0.84	0.025	$160.5° \pm 0.3°$	$158.5° \pm 0.7°$	$162.4° \pm 1.2°$

C2O8	0.89	0.021	$159.6° \pm 1.0°$	$158.9° \pm 0.3°$	$162.8° \pm 0.7°$
C2O10	0.92	0.019	$158.8° \pm 0.5°$	$158.5° \pm 0.9°$	$162.5° \pm 0.8°$
Open-I35	1	0.013	$160.4° \pm 0.8°$	$157.7° \pm 1.1°$	$161.7° \pm 1.8°$
Open-I45	1	0.11	$158.3° \pm 1.1°$	$156.9° \pm 1.6°$	$162.5° \pm 0.1°$

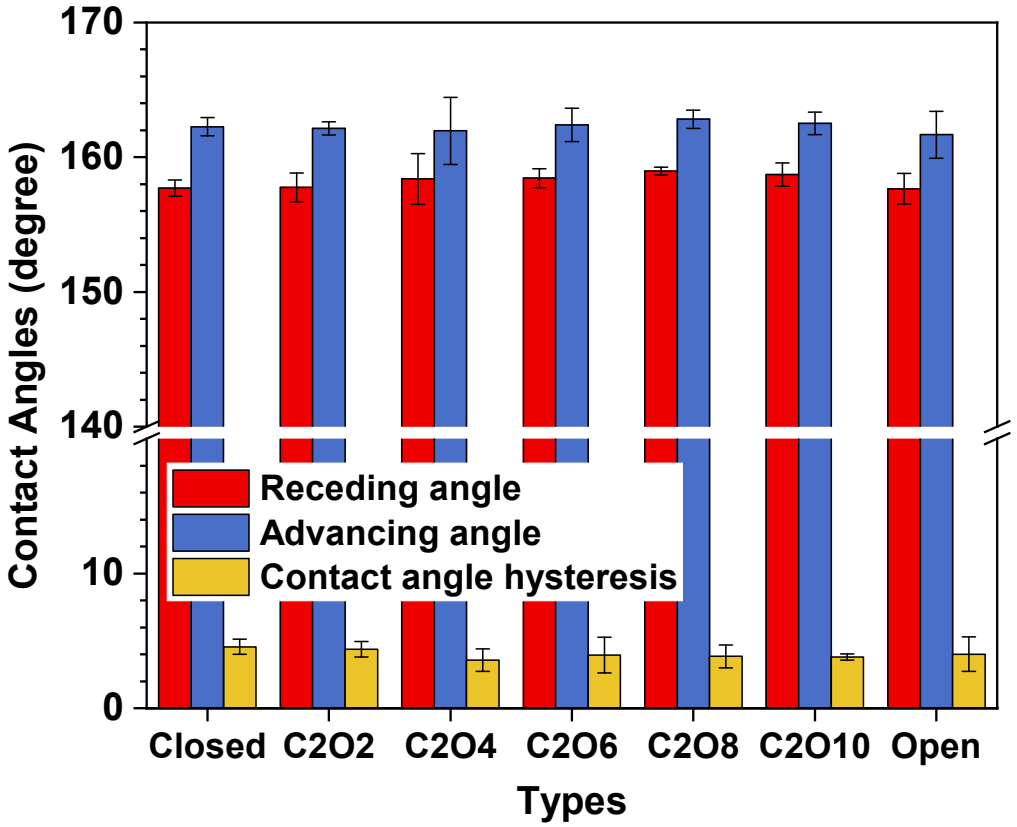

Fig. S2 Contact angles including receding angles, advancing angles and contact angle hysteresis. Data are mean ± s.d. from at least three independent measurements.

S3. Superhydrophobic durability tests of different patterned surfaces at room temperatures

Linear abrasion tests were performed to examine the superhydrophobic durability of different surfaces. The ambient temperature and humidity during tests are 15 ± 1 °C and 20 ± 5%. 300 grit sandpapers (727 CW) were adopted to abrade the surfaces under the loaded pressures of 12.25 kPa. One abrasion cycle was defined as a 20 cm motion of the measured surfaces on the abrasives.

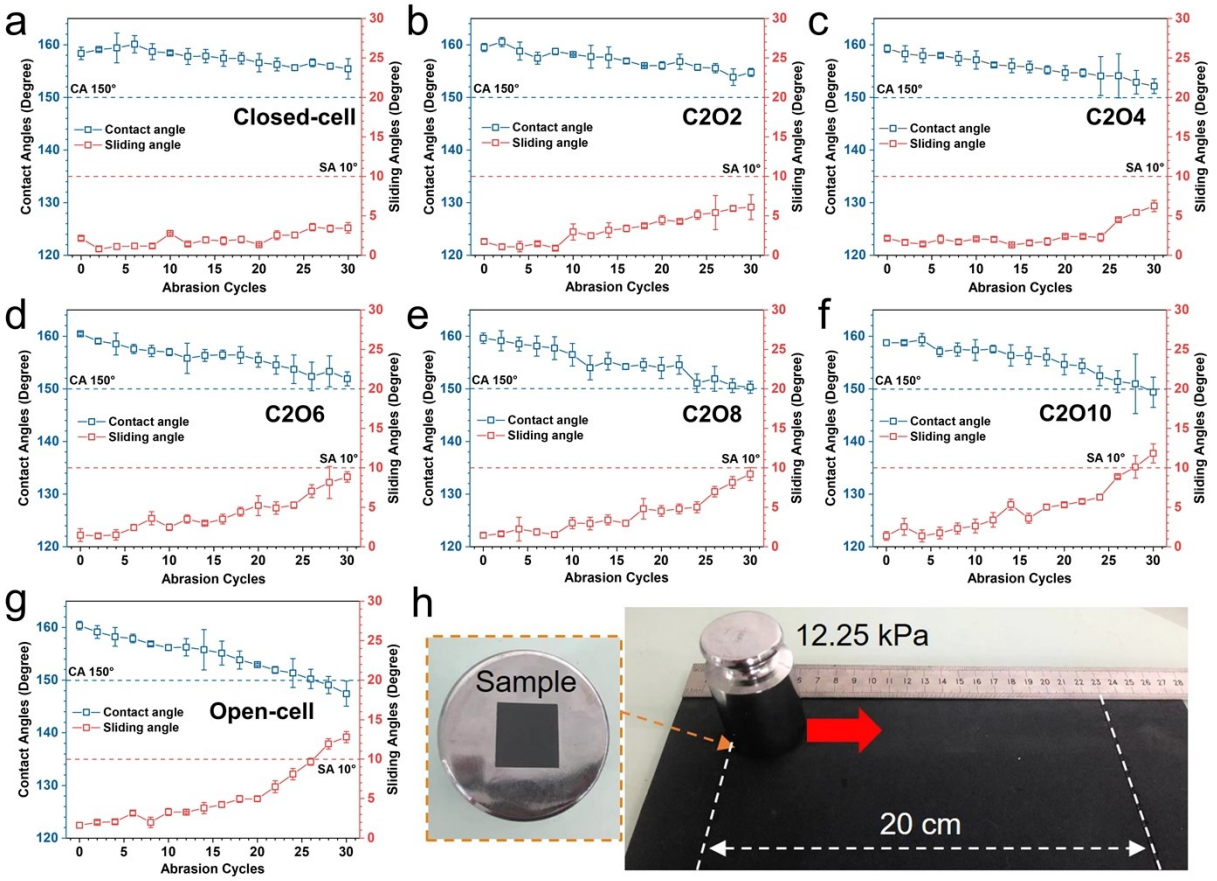

Fig. S3 Superhydrophobic durability tests of different surfaces at room temperatures. (a) Closed-cell surfaces. (b) C2O2 surfaces. (c) C2O4 surfaces. (d) C2O6 surfaces. (e) C2O8 surfaces. (f) C2O10 surfaces. (g) Open-cell

surfaces. (h) Photographs of durability experiment processes. The superhydrophobic evaluation standards with contact angles of more than 150° and sliding angles of less than 10° are marked in the figures. The linear abrasion direction and the abrasion distance are also shown. Data are mean ± s.d. from at least three independent measurements.

S4. Constructed thermodynamically closed systems and open systems on patterned surfaces

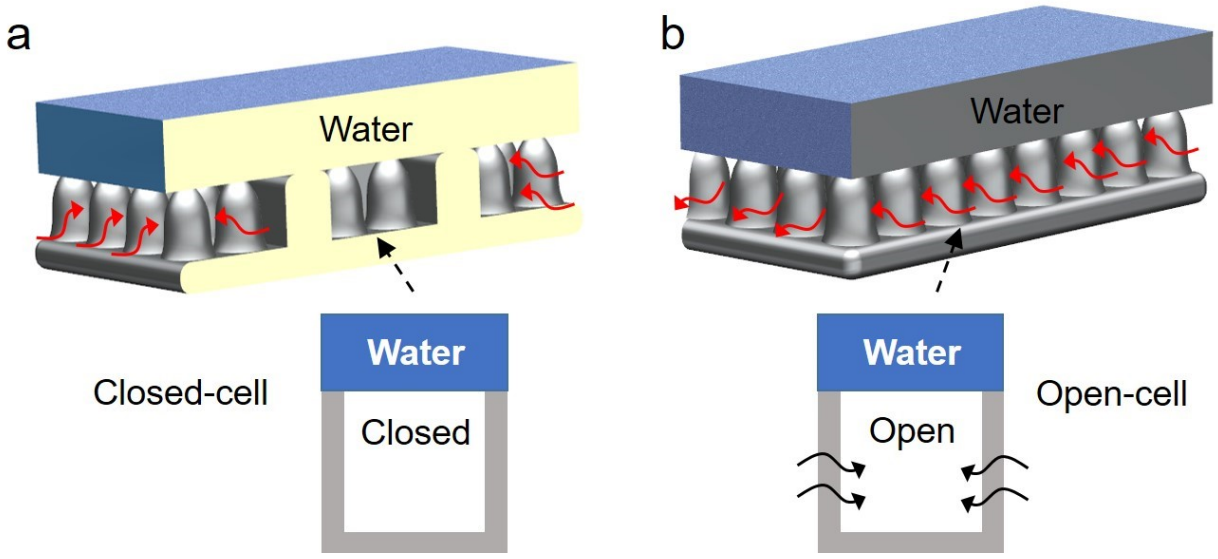

Fig. S4 Comparison of the closed-cell structures and the open-cell structures. (a) C2O2 surfaces consisting of open-cell structures and closed-cell structures. (b) Open-cell surfaces. In open-cell structures, air can freely flow and exchange, forming thermodynamically open systems. While in the closed-cell structures, the air pocket gas is restricted in the closed system, unable to be supplied from the ambient atmosphere. The corresponding schematics are shown. Red and black arrows denote the directions of gas flowing.

S5. Icing & melting cycles on different patterned surfaces

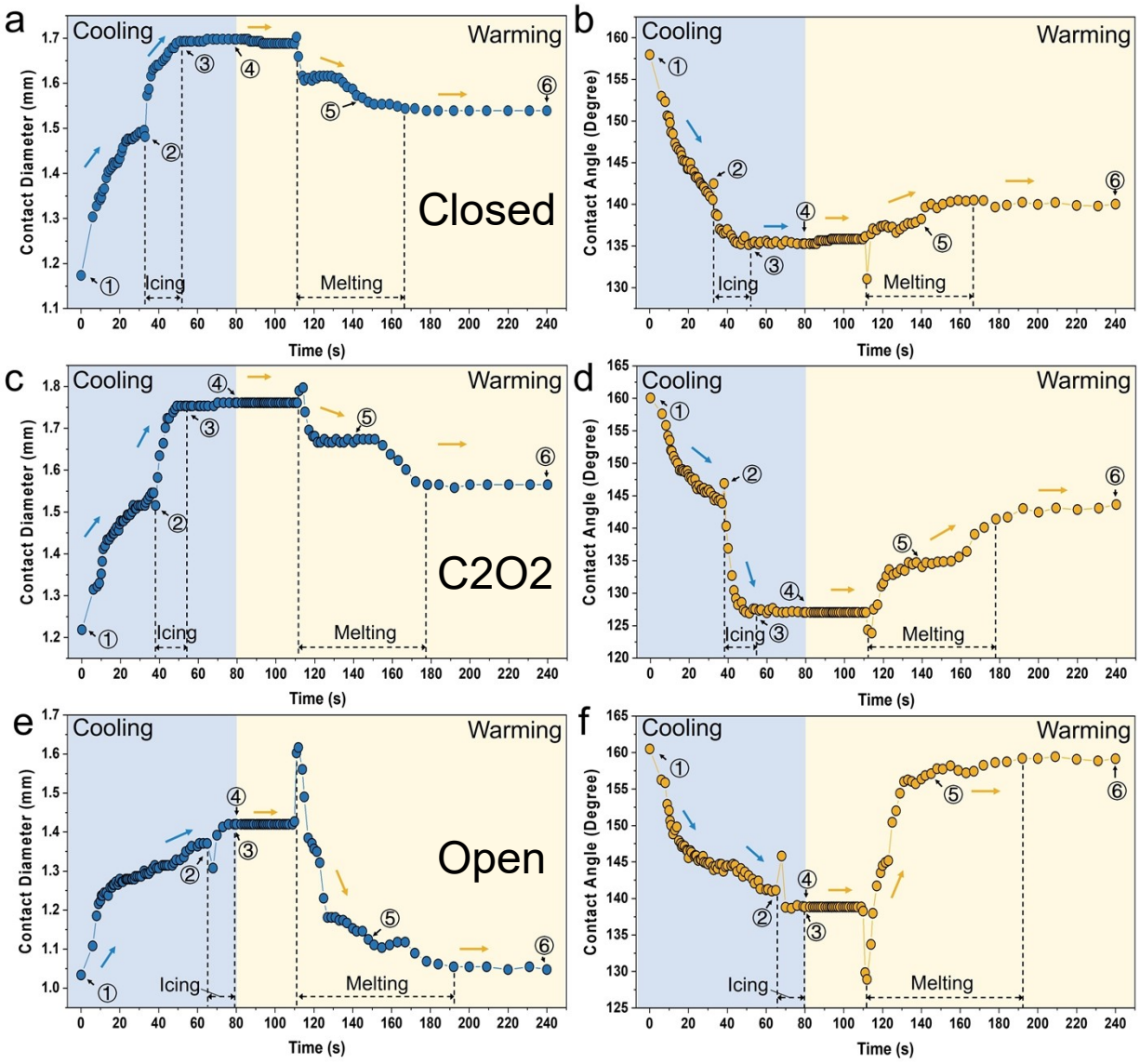

Fig. S5 Contact diameters and contact angles versus icing & melting cycle time: (a-b) Closed-cell surfaces; (c-d) C2O2 surfaces; (e-f) Open-cell surfaces. The blue zone denotes the icing processes while the orange zone denotes the melting processes. Icing zones and melting zones are divided by black dashed lines. Blue arrows and orange arrows denote the circulation directions of icing processes and melting processes, respectively. The

marked different states are corresponded to the droplet states in Figure 2. The fluctuations of the correlation evaluations are described in the Experimental section.

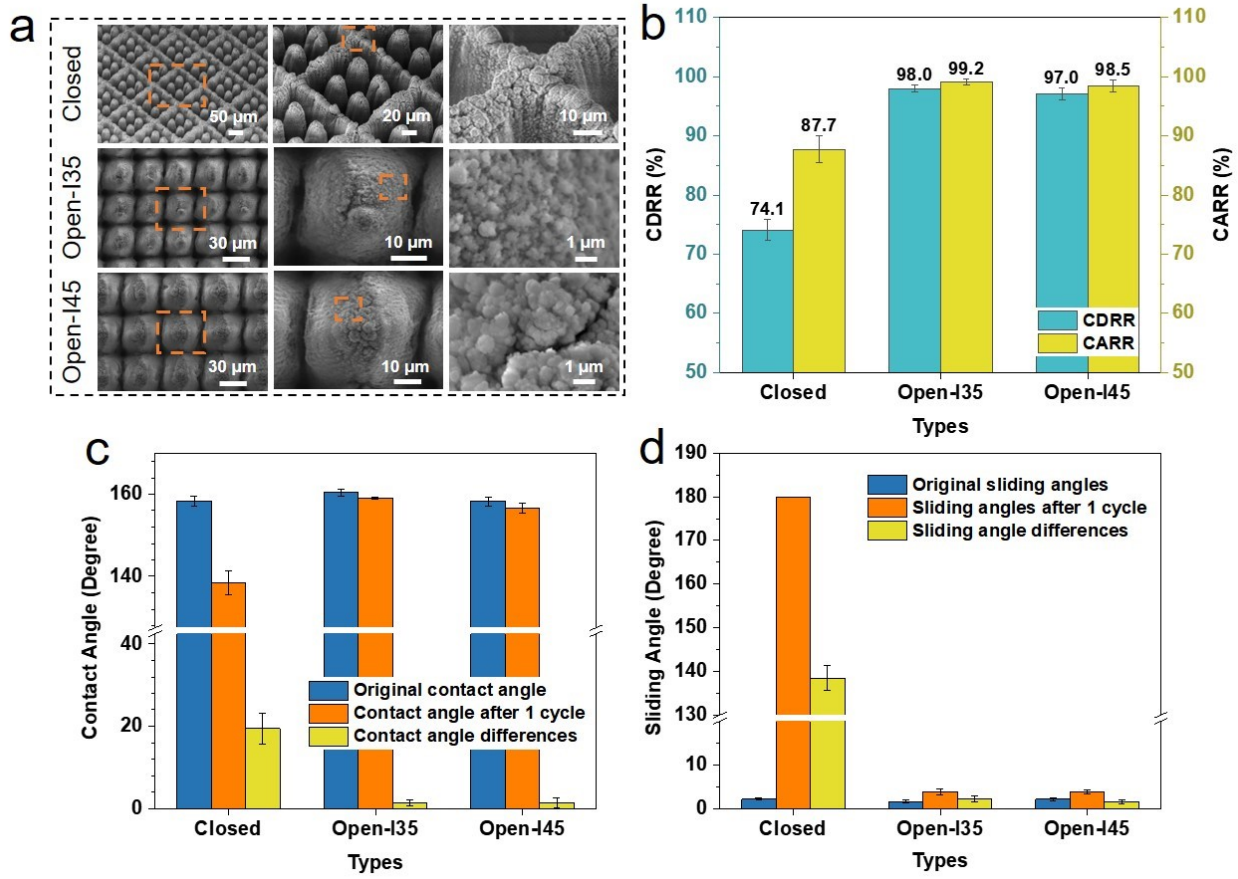

Fig. S6 Icing & melting cycle tests on micro-nanostructured surfaces with similar solid fractions but different patterns. (a) SEM images of the closed-cell surfaces (f = 0.081), open-I35 surfaces (f = 0.013) and open-I45 surfaces (f = 0.11). (b) CDRR and CARR of different surfaces after icing & melting cycles. (c) and (d) denote the changes of contact angles and sliding angles during icing & melting cycles, respectively. Data are mean ± s.d. from at least three independent measurements.

S6. Calculation of air pocket pressures on the open-cell structures and the closed-cell structures

The air pocket pressure on the open-cell structures can be calculated by:

$$P_{apo} = P_0 ln \frac{H_p}{H_p - (H_m^{eff})_{max}} \tag{S2}$$

$$(H_m^{eff})_{max} = \frac{f_1}{(1-f_1)}\left(\sqrt{\frac{\pi}{2f_1}} - 1\right)^3 (H_m)_{max} \tag{S3}$$

$$H_m^{eff} = \frac{r_{eff}^{g}(2 - 3sin\alpha_1 + sin^3\alpha_1)}{-3cos^3\alpha_1} \tag{S4}$$

$$r_{eff}^{g} = (\sqrt{\pi/2f_1} - 1)r_p \tag{S5}$$

where r_{eff}^{g} denotes the equivalent geometric radius for hierarchically structured surfaces with pillars, respectively; f_1 is the area fraction of micropillars, which is 0.16 in this work; r_p is the pillar radius, which is 7.9 μm in this work; α_1 denotes the sag angle of the liquid-vapor interface; P_{apo} is the pressure of trapped air pockets in closed-cell systems; P_0 denotes the ambient air pressure, which keeps the constant value ($1.0135 \times 10^5\ Pa$ at 15 ℃) in the closed-cell systems but varies as the ambient temperature changes in open-cell systems, $P_0 = 1.04 - 2.69 \times 10^{-12} e^{T/1.44} - 0.016 e^{T/37.29}\ bar$; T is the temperature of the air pocket; H_p is the pillar height; H_m^{eff} is the equivalent value of H_m; H_m is the meniscus height; $(H_m^{eff})_{max}$ denotes the maximum of H_m^{eff}, where α_1 is equal to θ_{adv}.

Different from the open-cell structures, the dissolution of air pocket gas in supercooled droplets on the closed-cell structures can lead to the decrease of gas amount. Meanwhile, P_0 on the closed-cell structures is the original atmospheric pressure before the icing & melting cycle, which is different from that on the open-cell structures. Hence considering these factors, the air pocket pressure on the closed-cell structures is expressed by:

$$\begin{cases} P_{c0}V_{c0} = \dfrac{V_{c0}}{V_m}RT_0 \\ P_{apc}V_{c0} = \dfrac{V_{c0} - V_{c0}[\alpha(T) - \alpha(T_0)]}{V_m}RT \end{cases} \tag{S6}$$

where P_{c0} denotes the pressure of trapped air pockets in the original state of the closed-cell; V_{c0} is the volume of the air pocket; V_m is the molar volume of gas; R is the ideal gas constant; T_0 is the original ambient temperature; P_{apc} is the pressure of air pockets in the closed-cell systems; $\alpha(T)$ is the air solubility in water, $\alpha(T) = A + BT + CT^2 = (29 - 0.7T + 0.008T^2) \times 10^{-3}$; r_c is the effective radius in the closed-cell, which is $31.8\ \mu m$ in this work. By simplifying eq S5, the below equation is obtained:

$$P_{apc} = P_{c0}\{1 - [\alpha(T) - \alpha(T_0)]\}\frac{T}{T_0} \tag{S7}$$

For the air pocket pressure in the original state of the closed-cell structures, it can be calculated by:

$$P_{c0} = P_0 ln\frac{H_p}{H_p - (H_m)_{max}} \tag{S8}$$

$$H_m = \frac{r_c(2 - 3sin\alpha_1 + sin^3\alpha_1)}{-3cos^3\alpha_1} \tag{S9}$$

Combining eq S6-9, the air pocket pressure on the closed-cell structures is expressed by:

$$P_{apc} = P_0 ln \frac{H_p}{H_p - (H_m)_{max}} \{1 - (T - T_0)[B + C(T + T_0)]\} \frac{T}{T_0} \tag{S10}$$

In terms of eq S2 and S10. The evolutions of air pocket pressure with the temperature and the ratio of the open-structural area to the total area of one cell (ROT) are obtained in Figure S7.

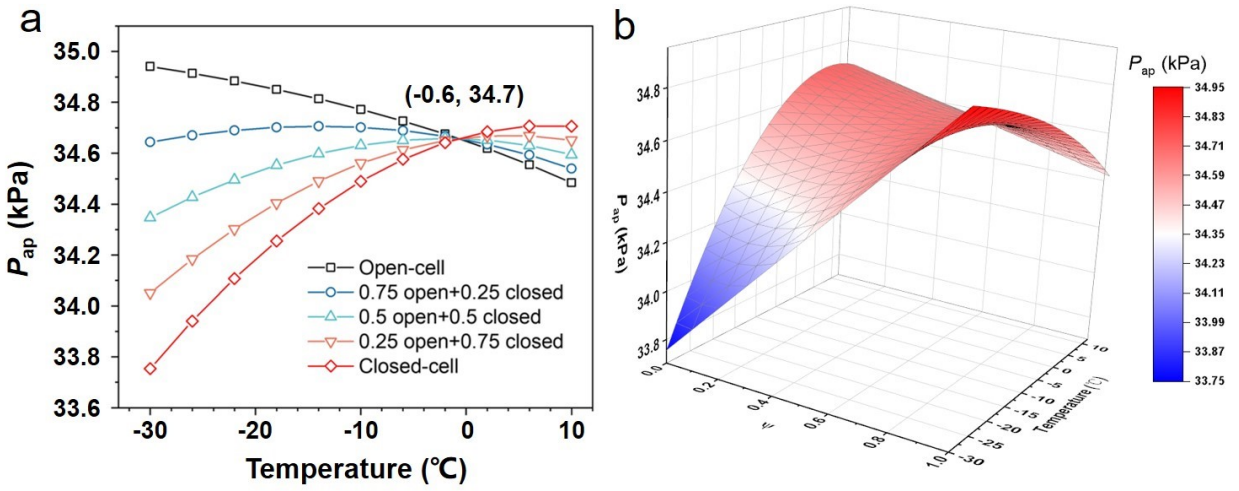

Fig. S7 Evolutions of air pocket pressure with the temperature and the ROTs. (a) The air pocket pressures at different temperatures and on the surfaces with different ROTs. (b) Three-dimension phase diagram.

S7. Calculation of interfacial thermal resistances on different patterned surfaces

Based on quasi-static thermal current model, the thermal resistance of microstructures is expressed by eq S11, and that of air pocket layer is expressed by eq S12. The total interfacial thermal resistance is obtained in eq S13

$$R_s = \frac{1}{\pi r_d^2 f \cdot sin^2\theta}\left(\frac{\delta_c}{k_c} + \frac{\delta_m}{k_m}\right) \tag{S11}$$

$$R_a = \frac{1}{\pi r_d^2 (1-f) sin^2\theta} \cdot \frac{\delta_a}{k_a} \tag{S12}$$

$$R_{total} = \frac{\delta_a(k_m\delta_c + k_c\delta_m)}{\pi r_d^2 sin^2\theta[f k_c k_m \delta_a + (1-f)k_a(k_m\delta_c + k_c\delta_m)]} \tag{S13}$$

where R_s and R_a are the thermal resistances of solid microstructures and air pocket layer, respectively; R_{total} is the total thermal resistance; r_d is the droplet radius; f is the surface solid fraction; θ denotes the apparent contact angle; δ_c, δ_m and δ_a denote the thickness of superhydrophobic coatings, microstructures and the air pocket layer; k_c, k_m and k_a denote the thermal conductivity of superhydrophobic coatings, microstructures and the air pocket layer. In

our work, $\delta_c = 10\ nm$, $\delta_m = \delta_a = 45\ \mu m$, $k_c = 0.1\ W \cdot m^{-1} \cdot K^{-1}$, $k_m = 154.11\ W \cdot m^{-1} \cdot K^{-1}$. Figure S8 shows the interfacial thermal resistances on different surfaces.

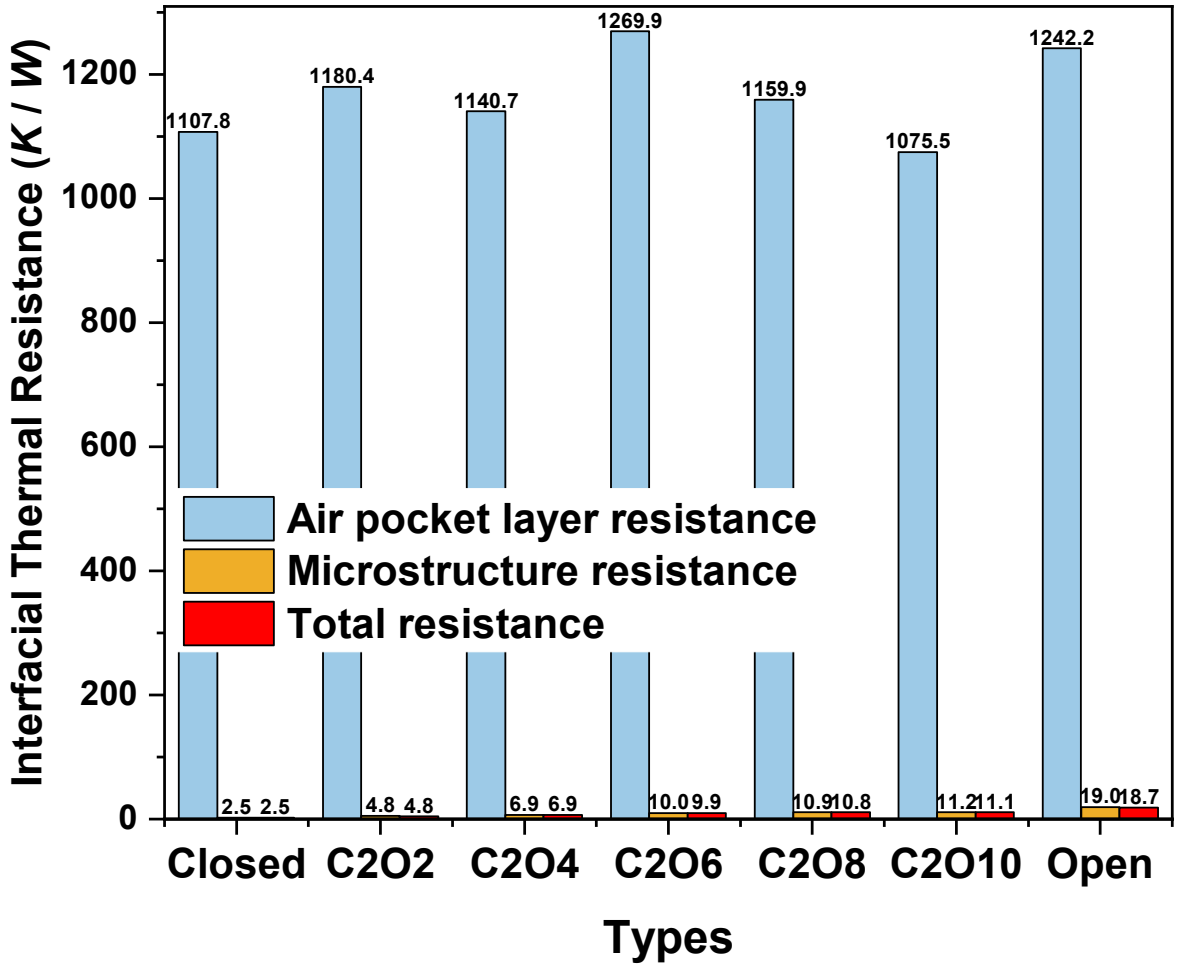

Fig. S8 Interfacial thermal resistances between droplets and different surfaces.

S8. Calculation of total bubbles volume in the ice droplet

Owing to the limitation of characterization devices, the datum of 3D bubbles in ice droplets cannot yet be constructed and obtained in experiments. However, by combing the theoretical calculations and experimental results, the total bubble volume in the ice droplets can still be obtained. The total bubbles volume is expressed as:

$$V_{tb} = \pi(1+\frac{1}{\nu\alpha})^{-1}\int_0^t [(r_d^2 \sin^2\theta - 2S_t D\cdot t - 2r_d(2S_t D\cdot t)^{1/2}\cos\theta)\cdot(\frac{S_t D}{2t})^{1/2}]dt \quad \text{(S14)}$$

While V denotes the density ratio of ice and water, in this work, we take 0.92; α is the air solubility in the supercooled water, which takes 3.6%, 4.4%, 5.04% when the temperature of the supercooled water is -5 ℃, -10 ℃, -15 ℃, respectively; S_t denotes the Stefan number, $S_t = C_p\Delta T_c/L_m$; D is the thermal diffusivity, $D = \lambda_{ice}/(\rho_{ice}C_p)$; t denotes the icing time, recorded from the beginning of icing; C_p represents the heat capacity at the constant pressure; ΔT_c is the supercooled temperature; L_m is the latent heat during the freezing processes; ρ_{ice} is the ice density; λ_{ice} is the thermal conductivity of ice.

S9. Icing & melting cycle tests on copper substrates

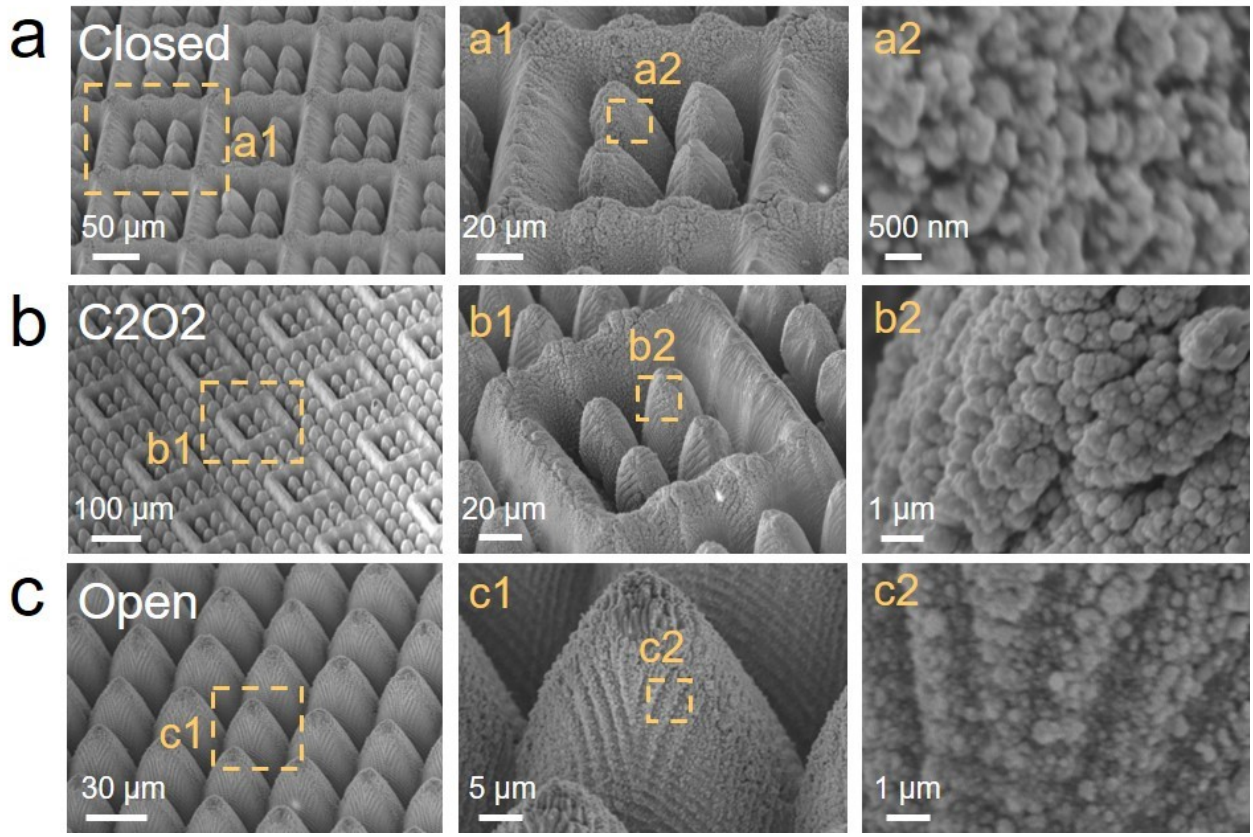

Fig. S9 SEM images of three patterns on copper substrates: open-cell, C2O2 and closed-cell.

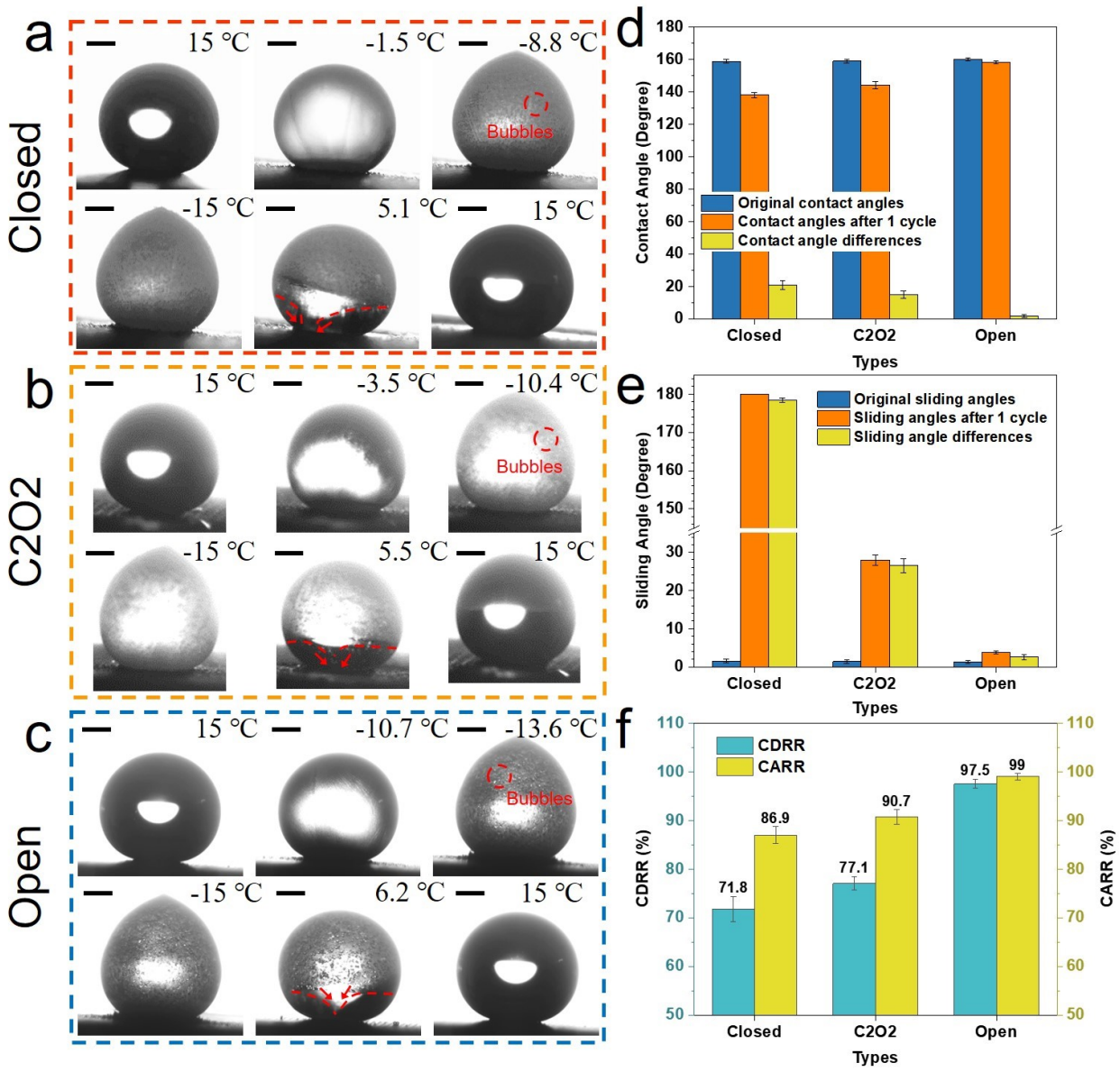

Fig. S10 Icing & melting cycle results on the copper patterned substrates. (a-c) Droplet state changes during cycles: (a) closed-cell; (b) C2O2; (c) open-cell. Scale bars are 500 μm. (d) and (e) denote changes of contact angles and sliding angles during icing & melting cycles, respectively. (f) CDRR and CARR of different surfaces. The tested copper samples have the high thermal conductivity of $397\ W \cdot m^{-1}K^{-1}$. Data are mean ± s.d. from at least three independent measurements.

S10. Durability analyses of different patterned surfaces after multiple deicing cycles

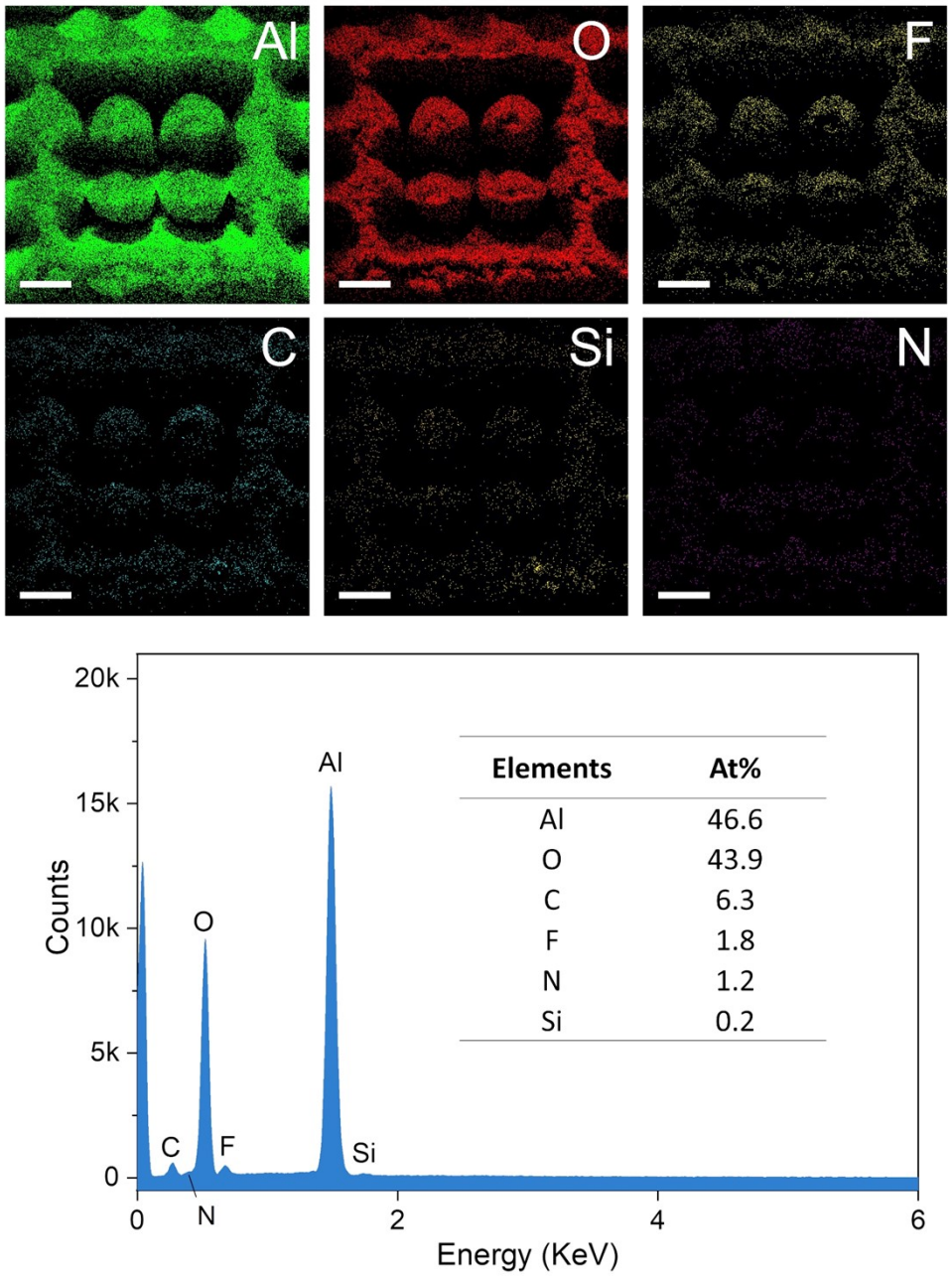

Fig. S11 EDS mappings and elemental ratios on the closed-cell structures after 10 deicing cycles. It can be clearly observed that the elements of F and C on the tops of microframes and microcones have been greatly lost, which leads to the deterioration of superhydrophobicity and icephobicity. Scale bars are 25 μm.

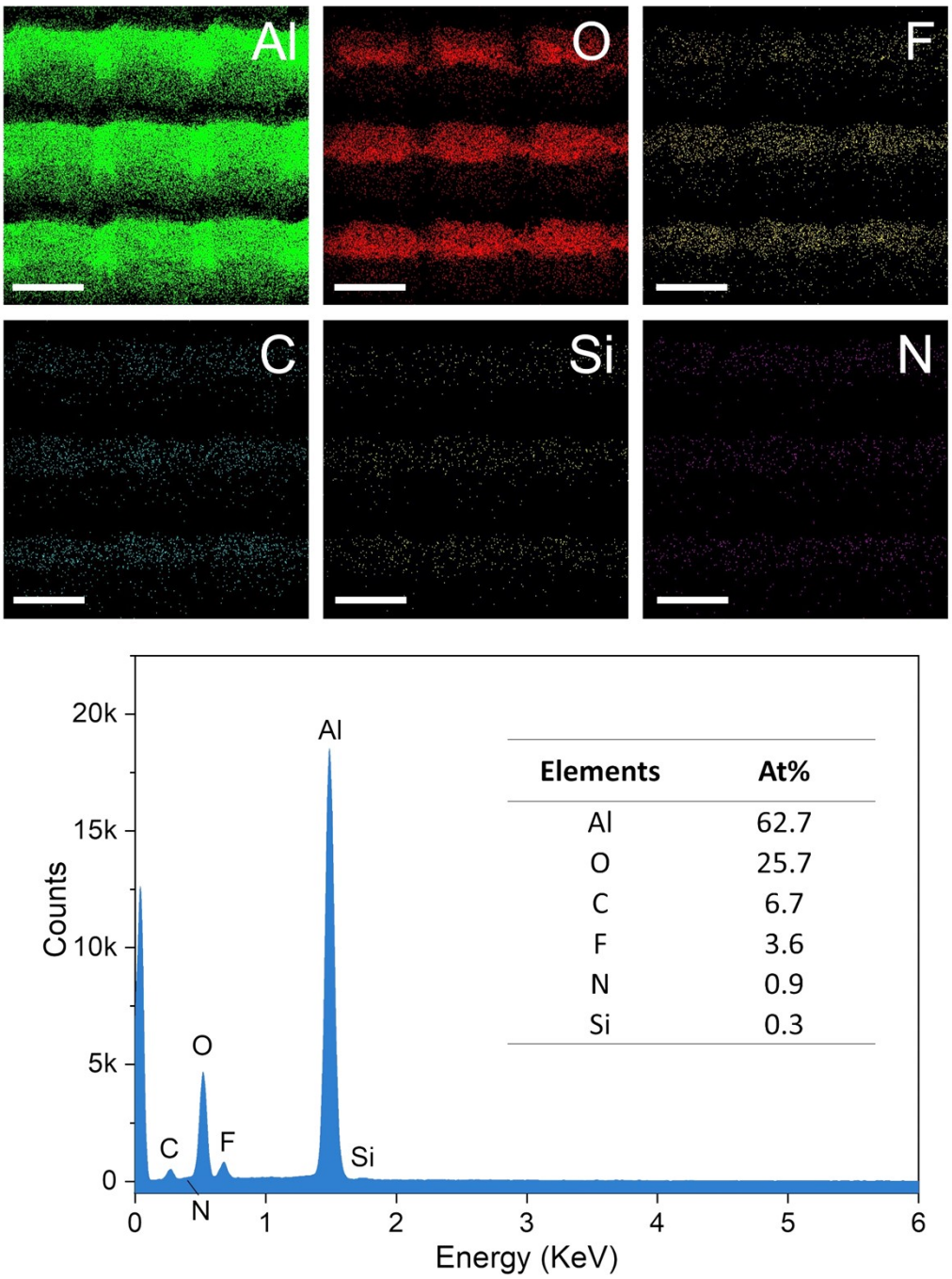

Fig. S12 EDS mappings and elemental ratios on the open-cell structures after 10 deicing cycles. It is found that the elements on the open-cell structures have no obvious variation. Abundant F and C elements after 10 deicing cycles ensure the well icephobic durability of open-cell surfaces. Scale bars are 25 μm.

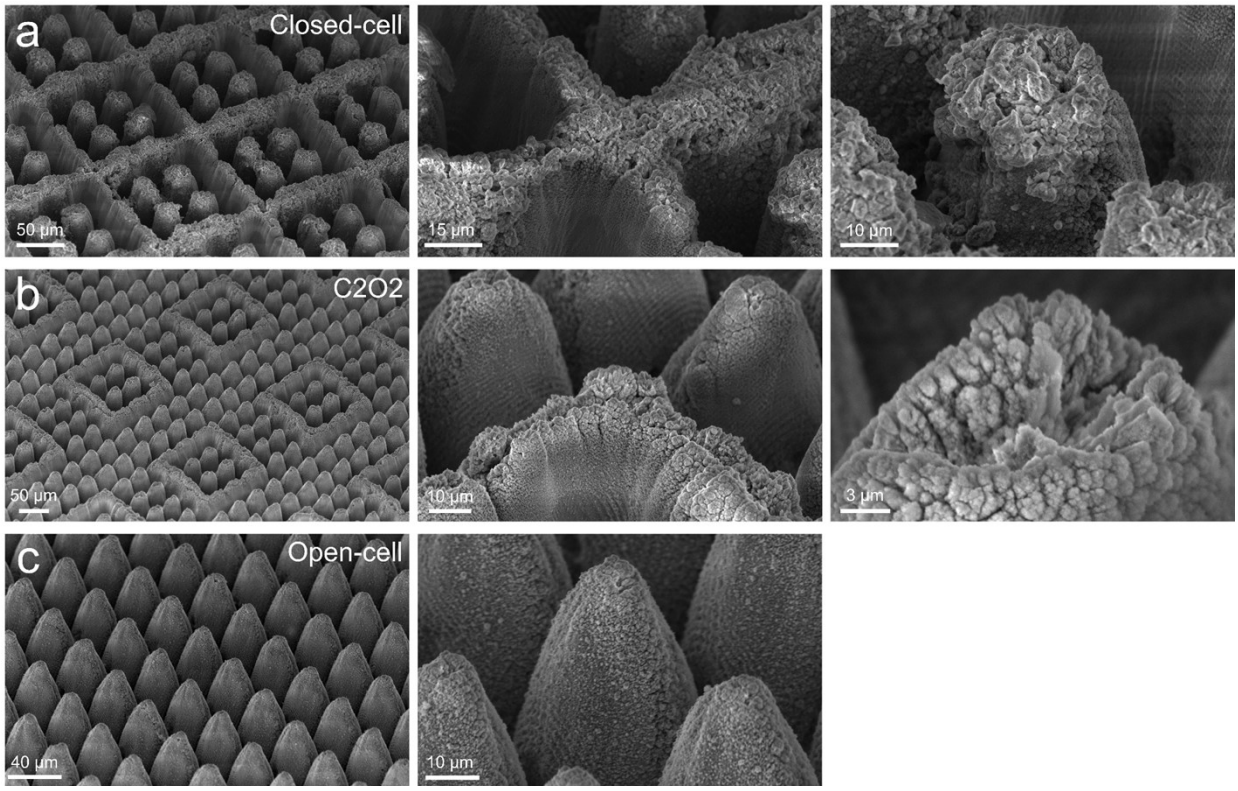

Fig. S13 SEM images of different patterned surfaces after 10 deicing cycles. (a) Closed-cell surfaces. (b) C2O2 surfaces. (c) Open-cell surfaces. After 10 deicing cycles, the microframes and the enclosed microcones on the closed-cell surfaces have been greatly damaged. On the C2O2 surfaces, although the microframes and their enclosed microcones are also abrased, the open microcones outside the microframes have no obvious damage. Meanwhile, it can be apparently observed that the micro-nanostructures on the open-cell surfaces remain intact. The undamaged micro-nanostructures and chemical elements on the open-cell surfaces guarantee the ice easy-removal after multiple deicing cycles.

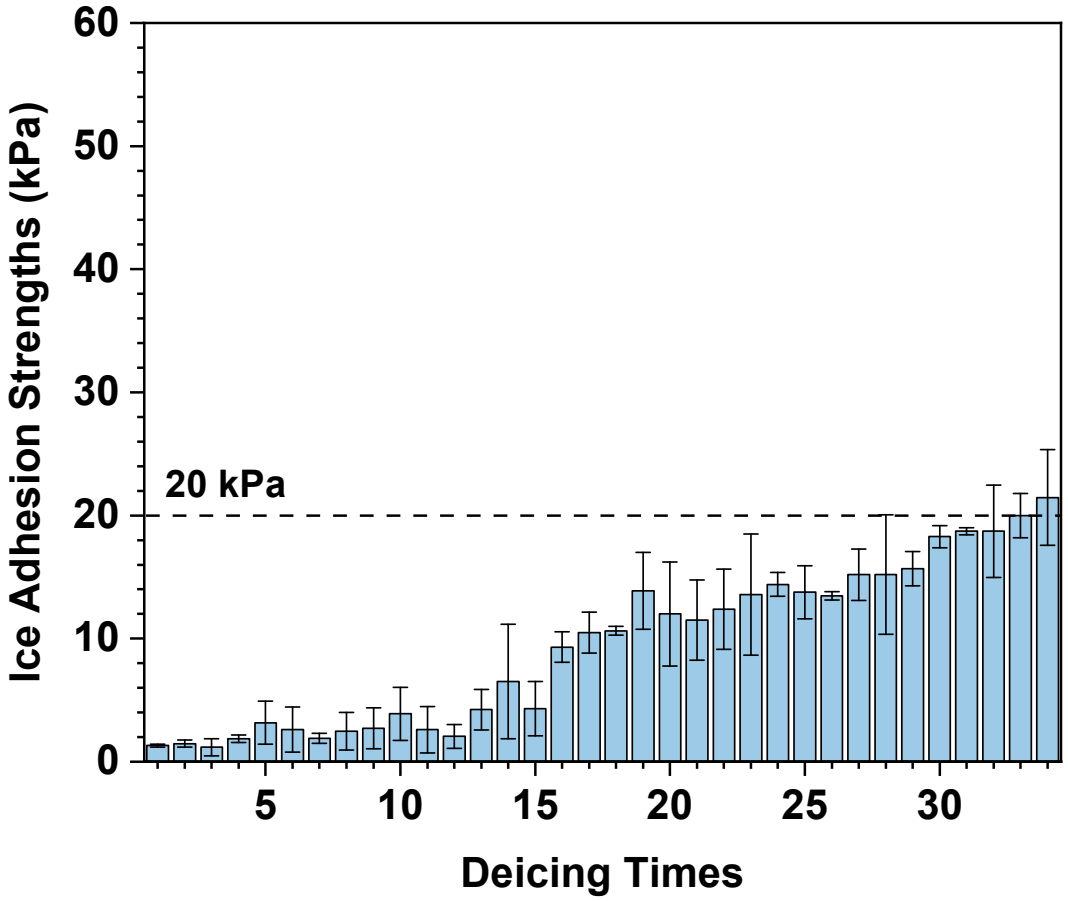

Fig. S14 Icephobic durability tests on the open-cell surfaces. Generally, 20 kPa is regarded as the benchmark for ensuring passive ice removal under external wind blow or slight vibration. It can be found that even after 33 deicing cycles, the ice adhesion strengths on the open-cell surfaces can still maintain below 20 kPa, well guaranteeing the long-term icephobicity. Data are mean ± s.d. from at least three independent measurements.

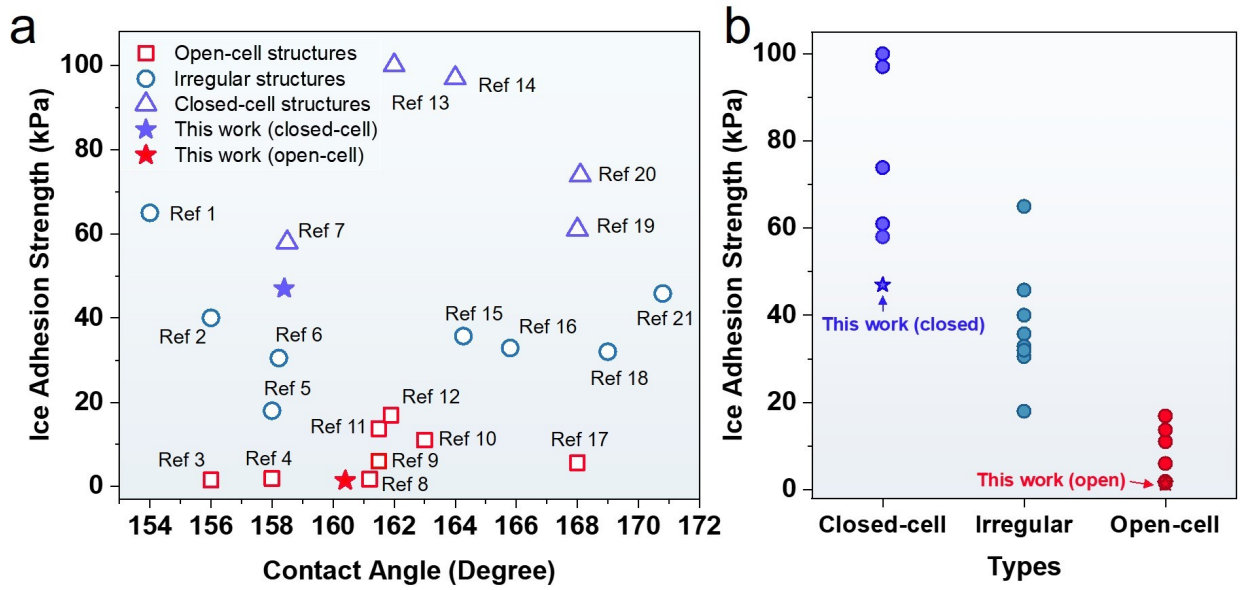

Fig. S15 Comparison of ice adhesion strengths between our fabricated surfaces and other reported superhydrophobic surfaces. (a) Ice adhesion strengths versus water contact angles. Red boxes, blue rounds and purple triangles denote the reported open-cell, irregular and closed-cell surfaces, respectively. Red and purple five-pointed stars denote our fabricated open-cell and closed-cell surfaces. (b) Ice adhesion strengths of different types of surfaces. Data is taken from the literature[1-21].

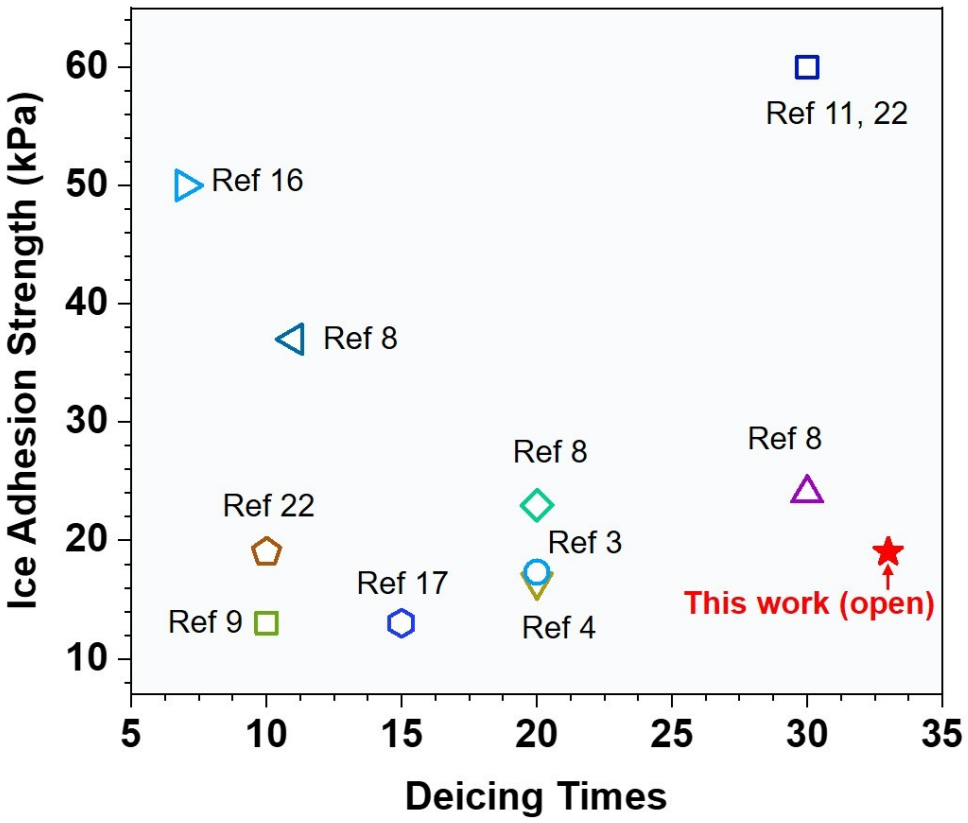

Fig. S16 Comparison of ice adhesion strengths after multiple deicing times between our fabricated surfaces and other reported superhydrophobic surfaces. Red five-pointed stars denotes our fabricated open-cell surfaces. Data is taken from the literature[3, 4, 8, 9, 11, 16, 17, 22].

S11. Observations of condensation processes on open-cell structures.

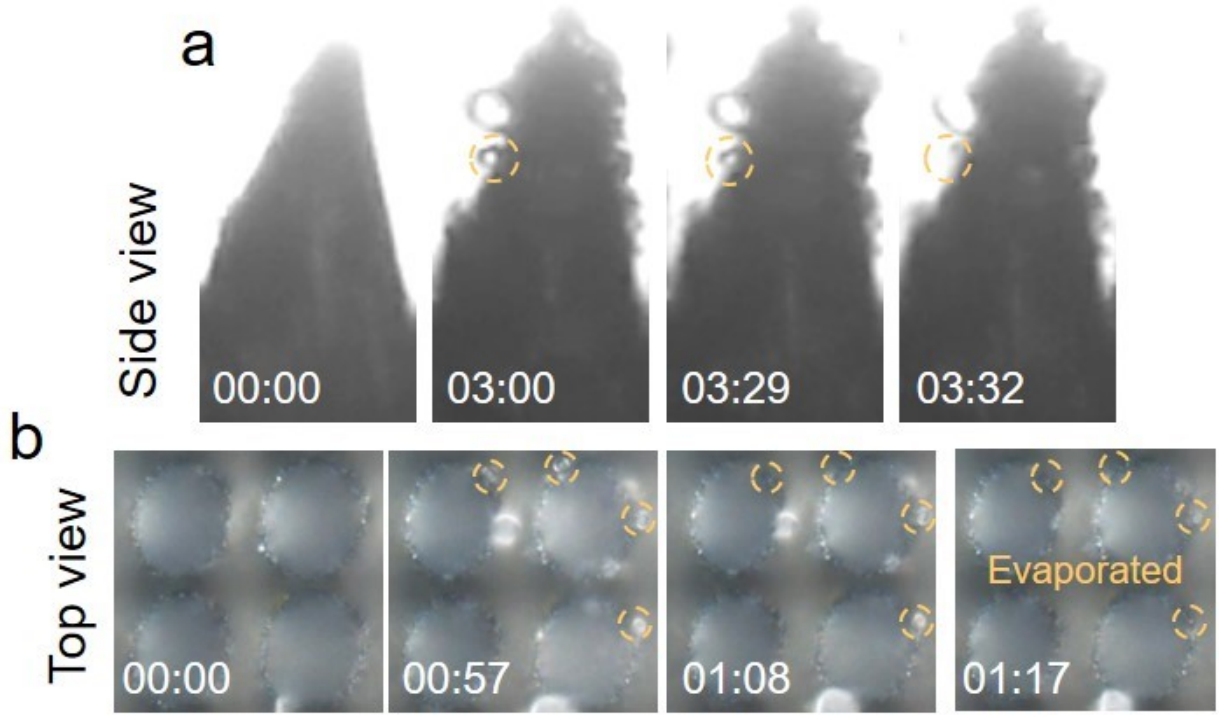

Fig. S17 Side and Top observations of condensation processes on open-cell structures. (a) Side view. (b) Top view. Condensates are marked by yellow dashed rounds. The recorded time is also displayed. The experimental methods are described in Experimental sections, which are same as those in Figure 6.

References

S1. S. A. Kulinich and M. Farzaneh, *Langmuir*, 2009, **25**, 8854-8856.

S2. S. Zheng, C. Li, Q. Fu, T. Xiang, W. Hu, J. Wang, S. Ding, P. Liu and Z. Chen, *RSC Advances*, 2016, **6**, 79389-79400.

S3. C. Chen, Z. Tian, X. Luo, G. Jiang, X. Hu, L. Wang, R. Peng, H. Zhang and M. Zhong, *ACS Applied Materials & Interfaces*, 2022, **14**, 23973-23982.

S4. P. Wang, Z. Li, Q. Xie, W. Duan, X. Zhang and H. Han, *Journal of Bionic Engineering*, 2021, **18**, 55-64.

S5. M. I. Jamil, X. Zhan, F. Chen, D. Cheng and Q. Zhang, *ACS Applied Materials & Interfaces*, 2019, **11**, 31532-31542.

S6. L. Pan, F. Wang, X. Pang, L. Zhang and J. Hao, *Journal of Materials Science*, 2019, **54**, 14728-14741.

S7. J. Ou, Q. Shi, Z. Wang, F. Wang, M. Xue, W. Li and G. Yan, *Science China Physics, Mechanics & Astronomy*, 2015, **58**, 1-8.

S8. R. Pan, H. Zhang and M. Zhong, *ACS Applied Materials & Interfaces*, 2021, **13**, 1743-1753.

S9. R. Pan, H. Zhang and M. Zhong, *Chinese Journal of Lasers*, 2021, **48**, 0202009.

S10. V. Vercillo, S. Tonnicchia, J.-M. Romano, A. García-Girón, A. I. Aguilar-Morales, S. Alamri, S. S. Dimov, T. Kunze, A. F. Lasagni and E. Bonaccurso, *Advanced Functional Materials*, 2020, **30**, 1910268.

S11. C. Chen, Z. Tian, X. Luo, G. Jiang, X. Hu, L. Wang, R. Peng, H. Zhang and M. Zhong, *Chemical Engineering Journal*, 2022, **450**, 137936.

S12. R. Pan, H. Zhang and M. Zhong, *ACS Applied Materials & Interfaces*, 2020, **13**.

S13. Z. Hong, M. Xue, Y. Luo, Z. Yin, C. Xie, J. Ou and F. Wang, *Journal of Applied Polymer Science*, 2021, **138**, 49657.

S14. N. Wang, L. Tang, W. Tong and D. Xiong, *Materials & Design*, 2018, **156**, 320-328.

S15. M. Jin, Y. Shen, X. Luo, J. Tao, Y. Xie, H. Chen and Y. Wu, *Applied Surface Science*, 2018, **455**, 883-890.

S16. K. Maghsoudi, E. Vazirinasab, G. Momen and R. Jafari, *Journal of Materials Processing Technology*, 2021, **288**, 116883.

S17. Y. Hou and K. L. Choy, *Progress in Organic Coatings*, 2022, **163**, 106637.

S18. V. Vercillo, DOI: 10.13140/RG.2.2.21398.47688, 2020.

S19. S. Milles, V. Vercillo, S. Alamri, A. I. Aguilar-Morales, T. Kunze, E. Bonaccurso and A. F. Lasagni, *Nanomaterials*, 2021, **11**, 135.

S20. H. Xie, X. Zhao, B. Li, J. Zhang, J. Wei and J. Zhang, *New Journal of Chemistry*, 2021, **45**, 10409-10417.

S21. X. Wu, Y. Shen, S. Zheng, Z.-T. Hu and Z. Chen, *Langmuir*, 2020, **36**, 12190-12201.

S22. Y. Zhao, Y. Liu, Q. Liu, W. Guo, L. Yang and D. Ge, *Materials Letters*, 2018, **233**, 263-266.